

13th CIRP Conference on Photonic Technologies [LANE 2024], 15-19 September 2024, Fürth, Germany

Describing the effect of local gas flow on keyhole and melt flow dynamics utilizing high-speed synchrotron X-ray imaging and numerical simulation

Leander Schmidt^{a,*}, Raschid Azizy^a, Klaus Schrickler^a, Christian Diegel^a, Yunhui Chen^{b,c},
Alexander Rack^c, Jean Pierre Bergmann^a

^aProduction Technology Group, Technische Universität Ilmenau, Gustav-Kirchhoff-Platz 2, 98693 Ilmenau, Germany

^bSchool of Engineering, RMIT University, Melbourne, Australia

^cESRF – The European Synchrotron, Structure of Materials Group - ID19, F-38043 Grenoble Cedex 9, France

*Corresponding author. Tel.: +49-3677-69-3854; fax: +49-3677-69-1660. E-mail address: leander.schmidt@tu-ilmenau.de

Abstract

Laser beam welding with partial gas shielding using local gas flows has been shown to be very effective in reducing spatter, especially when welding high-alloy steels at high processing speeds (≥ 8 m/min). This paper examines the gas flow induced mechanical effect on keyhole geometry and correlating melt flow by means of a computational fluid dynamics analysis. Therefore, keyhole mode laser beam welding of AISI304 was modeled by using the volume of fluid method in FLOW-3D. The mechanical effect of the partial shielding was implemented by considering the gas flow induced dynamic pressure. By varying flow rates, a widening, and a reduction in fluctuation amplitude of the keyhole rear wall was detected. Furthermore, the melt flow dynamics were characterized by less flow velocity and melt movement. The results were validated by a visual comparison with high-speed synchrotron X-ray imaging, showing a high degree of agreement in modeling accuracy of the keyhole dynamics.

© 2024 The Authors. Published by Elsevier B.V.

This is an open access article under the CC BY-NC-ND license (<https://creativecommons.org/licenses/by-nc-nd/4.0>)

Peer-review under responsibility of the international review committee of the 13th CIRP Conference on Photonic Technologies [LANE 2024]

Keywords: laser beam welding; high-alloy steel; local gas supply; local gas flow, CFD simulation; X-ray imaging

1. Introduction

Spatter formation in laser beam welding of high-alloy steels is a major issue when welding at processing speeds that cause characteristics of the Single-Wave-Regime ($v_w \approx 10 - 12$ m/min) and Elongated-Keyhole-Regime ($v_w \approx 16$ m/min) according to [1, 2]. The use of a partial gas shielding by local gas flows directed towards the keyhole aperture has been shown to be very effective in reducing spatter in partial penetration welding [3, 4] and full penetration welding [5]. The general effect can be attributed to chemical-metallurgical and mechanical phenomena. Based on the partial shielding of oxygen, the growth and distribution of oxides and nitrides are affected, which has a significant impact on the flow velocity of surface-near melt flows, e.g. Marangoni convection [6]. On the other side, the oxygen shielding affects the surface tension that

is crucial for the formation of the keyhole [7] and spatter formation [8]. The mechanical effect of a local gas supply can be attributed to the gas flow-induced dynamic pressure p_{gas} that can be approximated using the calculation of the stagnation pressure (equation 1), including ρ_{gas} as gas density and v_{gas} as flow velocity of the gas.

$$p_{\text{gas}} = \frac{1}{2} \cdot \rho_{\text{gas}} \cdot v_{\text{gas}}^2 \quad (1)$$

Due to the quadratic exponentiation of the flow velocity v_{gas} , an increase in gas flow rate results in a significant increase in dynamic pressure. This effect has been observed by a widening of the keyhole aperture caused by dynamic pressures of $p_{\text{gas}} \approx 5 - 8$ kPa [9]. The gas flow-induced pressure profiles have been characterized, showing a displacement of the pressure maximum relative to the center of the nozzle [10].

The chemical-metallurgical and mechanical phenomena affect the pressure balance of the welding process, which is given by the ratio of keyhole-opening to keyhole-closing pressures (equation 2) [11, 12].

$$p_{\text{recoil}} + \Delta p_{\text{dp,v}} + p_{\text{gas}} = p_{\sigma} + p_h + p_{\text{dyn}} \quad (2)$$

The chemical-metallurgical effect leads to changes on the surface tension pressure p_{σ} and the hydrodynamic pressure p_{dyn} while the recoil pressure p_{recoil} , the differential vapor pressure $\Delta p_{\text{dp,v}}$ and the hydrostatic pressure p_h are kept almost constant. On the other hand, the gas flow-induced dynamic pressure p_{gas} represents the mechanical effect acting as additional term on the side of keyhole-opening pressures. However, this mechanical effect of the local gas flow on keyhole and melt pool dynamics has not been studied yet.

This study aims to characterize the mechanical effect of local gas flows resulting from the gas flow-induced dynamic pressure p_{gas} on the keyhole geometry, melt pool dynamics and associated spatter formation by numerical computational fluid dynamics (CFD) simulation, which allows a separate consideration of mechanical and chemical-metallurgical effects. The results were validated by means of experimental investigations using high-speed synchrotron X-ray imaging and high-speed videography.

2. Experimental

2.1. Numerical simulation

A three-dimensional CFD simulation was performed using FLOW-3D (version: 11.2 update 6) with WELD module (version: 2.4.1.2.9). The computational domain is shown in Fig. 1 and includes void region and sheet region. The model was symmetric along the X-Z plane and considered a zone of coarse and fine mesh to reduce the computational load. The model utilized the same physics and governing equations as described in [13]. Following, the model was based on the Navier-Stokes equations for the conservation of mass fraction, momentum, and energy, as well as the heat transport equation. The model also considered physics to account for melting, evaporation, and solidification as well as allows a free surface tracking using the Volume-of-Fluid (VoF) method. The effects of surface

tension and multiple reflections were also modeled, while angle-dependent Fresnel absorption was neglected. In contrast to [13], the laser beam was represented by a top-hat intensity distribution according to the equipment used in the experimental investigations (cf. section 2.2). The welding process was modeled with a stationary positioned laser and a moving specimen to allow a visual comparison between simulated and experimental results. A phantom component with infinite expansion in X-direction was used to consider the movement of the specimen at welding speed ($\overline{v_{\text{phantom}}} = -\overline{v_w}$). The mechanical effect of the local gas supply was implemented by an additional dynamic pressure p_{gas} applied on all elements enclosed in the “dynamic pressure zone”. The size, pressure value and angle of pressure attack of this region were adapted from experimental investigations (cf. section 2.2).

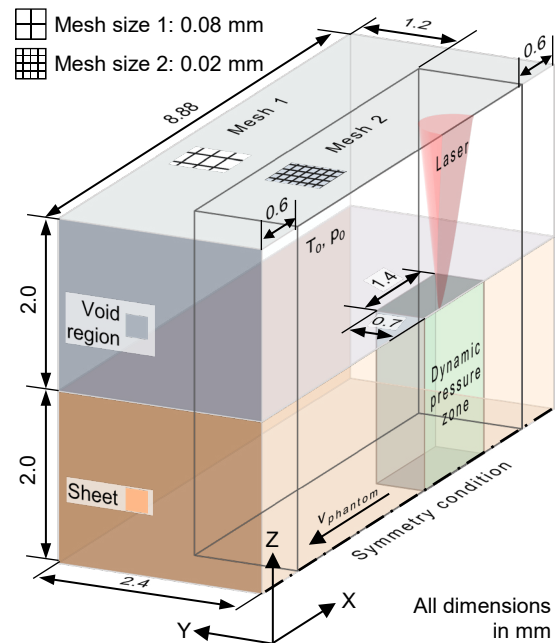


Fig. 2. Schematic of the computational domain used for numerical simulation.

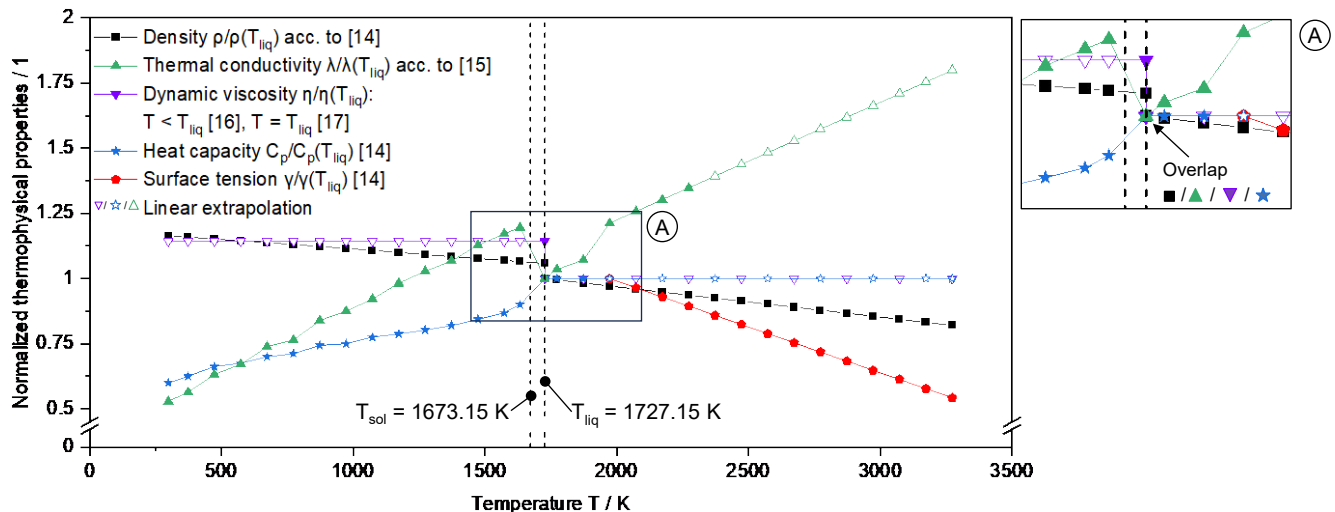


Fig. 1. Temperature-dependent data used for numerical simulation.

The model includes temperature-dependent data for density [14], thermal conductivity [15], dynamic viscosity [16, 17], heat capacity [14], and surface tension [14]. Fig. 2 shows the normalized thermophysical properties as a function of temperature based on the graphical representation of [18]. Missing data points were calculated by linear extrapolation. These points are indicated by outlined symbols (∇ / \star / \triangle). Other physical properties used are listed in Table 1.

Table 1. Constant physical properties of AISI 304 used for numerical simulation.

Physical property	Symbol	Value / unit	Ref.
Solidus temperature	T_{sol}	1673.15 K	[14]
Liquidus temperature	T_{liq}	1727.15 K	[14]
Shear Elastic Modulus	G	86 GPa	[19]
Tensile Strength, Yield	τ_y	215 MPa	[19]
Latent heat of vaporization	L_V	7600 kJ/kg	[20]
Accommodation coefficient	α	0.87	[21]

2.2. Experimental investigations

Partial penetration welds with a penetration depth of 1.7 mm were carried out on AISI 304 high-alloy steel at a welding speed of $v_w = 12$ m/min representing the Single-Wave-Regime for spatter formation. On the one hand, high-speed synchrotron X-ray imaging was performed to validate the numerical simulation. The experiments were carried out at beamline ID19 at the European Synchrotron Radiation Facility (see Fig. 3a). Vertically mounted steel sheets were welded and irradiated by a $4 \times 4 \text{ mm}^2$ X-ray beam with an energy $\leq 60 \text{ keV}$. The scintillator (Crytur, Ce-doped $\text{Lu}_3\text{Al}_5\text{O}_{12}$, thickness: $250 \mu\text{m}$) was lens-coupled to a Photron SA-Z high-speed camera (acquisition rate: 40,000 images/second, propagation distance: 4.5 m, $4 \mu\text{m}$ pixel size). A fiber laser ($\lambda = 1,070 \text{ nm}$) was used in the synchrotron experiments and the nominal tophat-intensity was adjusted to achieve the penetration depth addressed. Detailed information on the in situ X-ray imaging setup were presented in [6].

On the other hand, comparative experiments were performed for bead-on-plate welds using a Trumpf TruDisk 5000.75 disk laser ($\lambda = 1,030 \text{ nm}$) with a nominal focal diameter of $278 \mu\text{m}$ (see Fig. 3b). The process was recorded at 10,000 images/second using a Photron SA-X2 high-speed camera set at an angle of incidence of 60° to the sample surface. The camera was equipped with a Navitar 12X zoom lens system and a narrow-band filter with a center wavelength of 808 nm. The process was illuminated at a wavelength of 808 nm by a Cavitar Cavilux HF laser system.

Process gas was supplied locally by a gas nozzle with a constant diameter of 1.4 mm. The nozzle was mounted in 5 mm distance to the keyhole aperture in a trailing flow orientation at an angle of 48° relative to the sheet surface. Further details on the nozzle were described in [3, 5]. To separate mechanical and chemical-metallurgical effects, bottled air was used as process gas (supplier: Linde). Instead of shielding the weld from oxygen, as realized by using inert gases like argon, the use of compressed air does not significantly affect surface tension values and allowed the mechanical effect to be separated from

the chemical-metallurgical effect. The flow rate was controlled by a Bronkhorst FG-201AV-AGD-33-V-DA-000 mass flow controller. The gas-induced pressure was measured using the same procedure then described in [10] and used to set up the numerical simulation (cf. section 2.1).

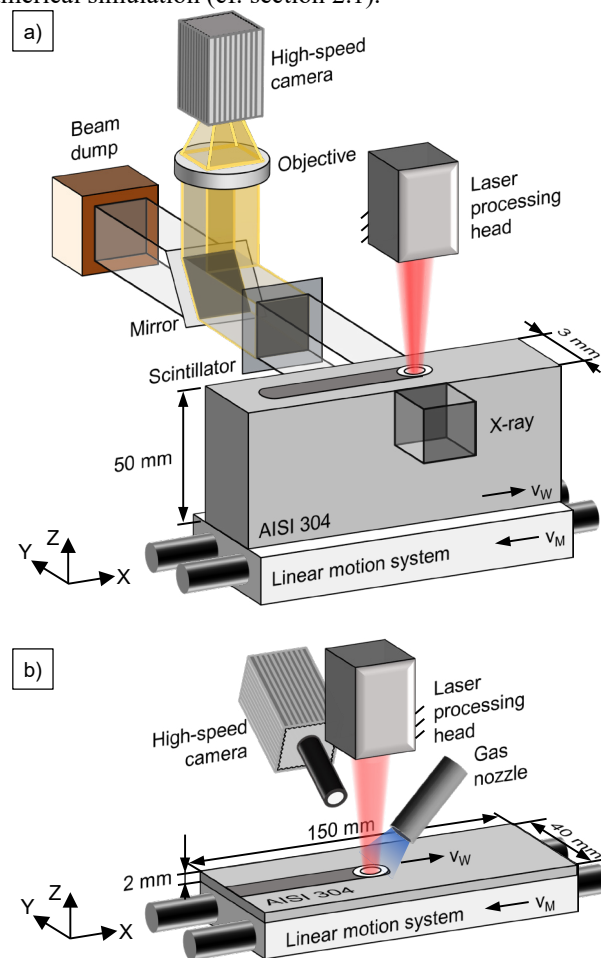


Fig. 3. (a) Setup for high-speed synchrotron X-ray imaging; (b) setup for high-speed videography of the welding process.

3. Results and discussion

3.1. Characterization of reference process

The first step focused on the characterization of the keyhole geometry and melt pool dynamics for welding high-alloy steel at a welding speed of $v_w = 12$ m/min without a local gas supply (reference process). The results are shown in Fig. 4.

The image series of the calculated temperature field (Fig. 4a) shows the formation of a keyhole with narrow aspect ratio, which is characterized by humps formed on the keyhole front. Based on local absorption and temperature maxima, these humps are moving downwards due to an induced recoil pressure [22]. As a result of strong fluctuations of the keyhole rear wall, the keyhole starts to neck at several positions, which occasionally results in the formation of pores due to a collapsing keyhole bottom (Fig. 4a, I). Subsequently, the keyhole depth was reestablished by a downward movement of the keyhole bottom (Fig. 4a, II), resulting in pore reabsorption in some images (Fig. 4a, III). At the same time, a melt pool

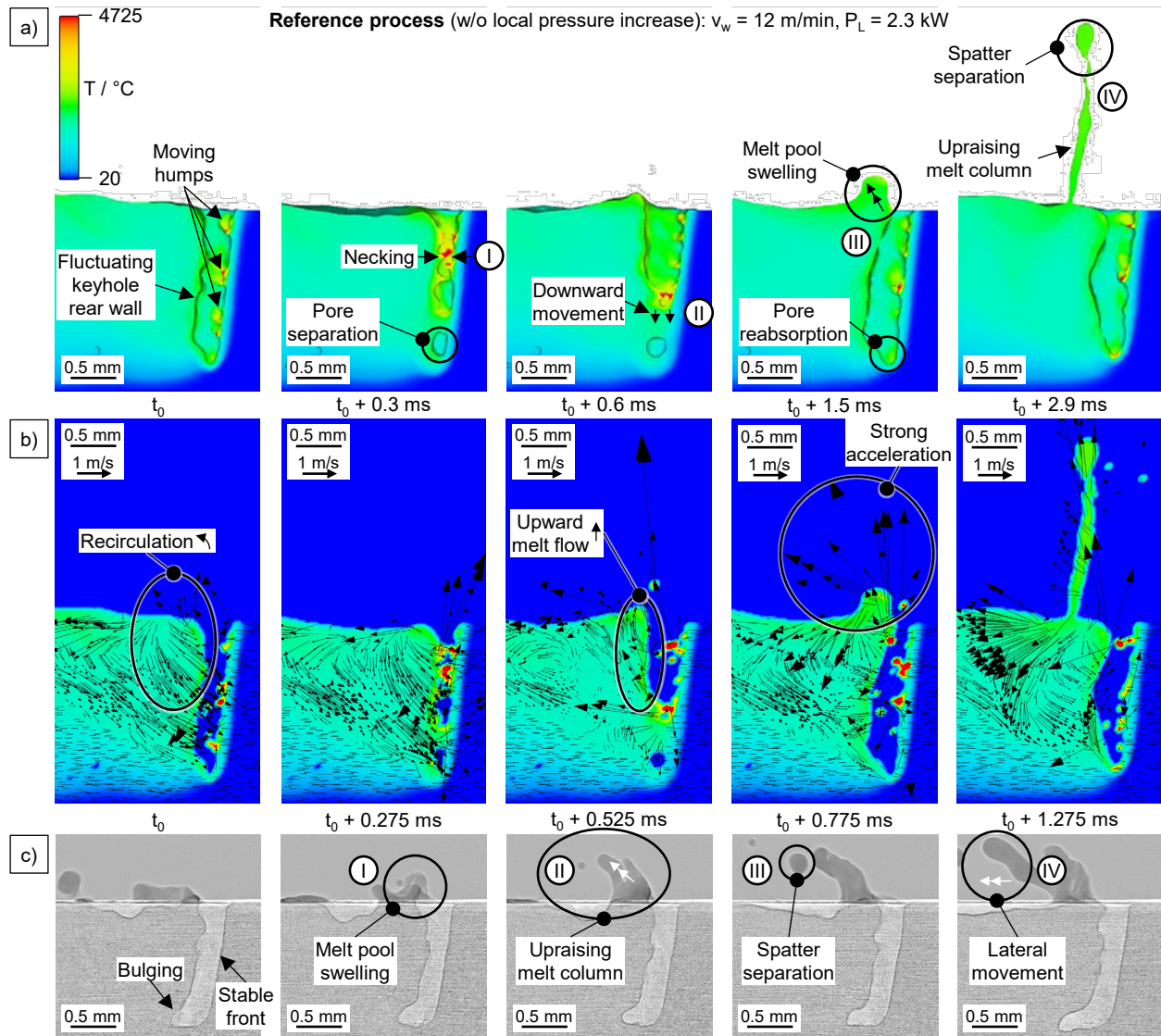


Fig. 4. Keyhole and melt pool dynamics of reference process: (a) temperature field; (b) overlay of temperature and X-Z flow field; (c) X-ray imaging.

swelling was formed on the upper keyhole rear wall. The upward movement caused the formation of a melt column that initiated the spatter detachment (Fig. 4a, IV). This behavior was accompanied by a change in melt pool dynamics (Fig. 4b). While the initial frame at t_0 showed the formation of a counterclockwise flow recirculation at the keyhole rear wall, the temporal necking of the keyhole resulted in an intensification of the upward melt flow at keyhole rear wall. As a result of this flow acceleration, the kinetic energy of the melt lead to the formation of an upward rising melt column and ultimately contributed to spatter detachment. The flow intensification also reinforced the recirculation at the keyhole rear wall. The high-speed synchrotron X-ray image series validates this behavior (Fig. 4c). The images also show the formation of a melt pool swelling in a first step (Fig. 4c, I), followed by a raising movement (Fig. 4c, II) and spatter separation (Fig. 4c, III). The melt column then moves laterally against the welding direction (Fig. 4c, IV). In contrast to the results of the numerical simulation, the high-speed synchrotron X-ray images show a less fluctuating keyhole front, no keyhole necking and the formation of a bottom-sided keyhole bulge. This can be attributed to the physical simplifications of FLOW-

3D, where the recoil pressure and recoil forces are considered to act only in the vertical Z-direction. However, the region of spatter detachment and the dynamics of the rear-sided melt pool swelling are very similar to the experiment, as are the underlying time scales. Since the dynamics of these regions are essential for spatter formation [1], this allows the model to be used to simulate the gas-induced local pressure increase next.

3.2. Effect of local pressure increase

The next step was to characterize the mechanical effect of a gas-induced pressure increase. While pressures of up to 300 mbar applied within the defined “dynamic pressure zone” resulted in marginally less fluctuation amplitude of the keyhole rear wall and a slight decrease in melt pool flow velocities, the following results are shown for a gas-induced pressure of $p_{\text{gas}} = 496 \text{ mbar}$, corresponding to a high flow rate setup ($\dot{V} > 25 \text{ l/min}$), to emphasize the fundamental effects. The image series of the temperature field (Fig. 5a) shows a lateral widening of the keyhole, while the keyhole rear wall was characterized by a very low fluctuation amplitude. Based on this behavior, spatter formation was significantly reduced by

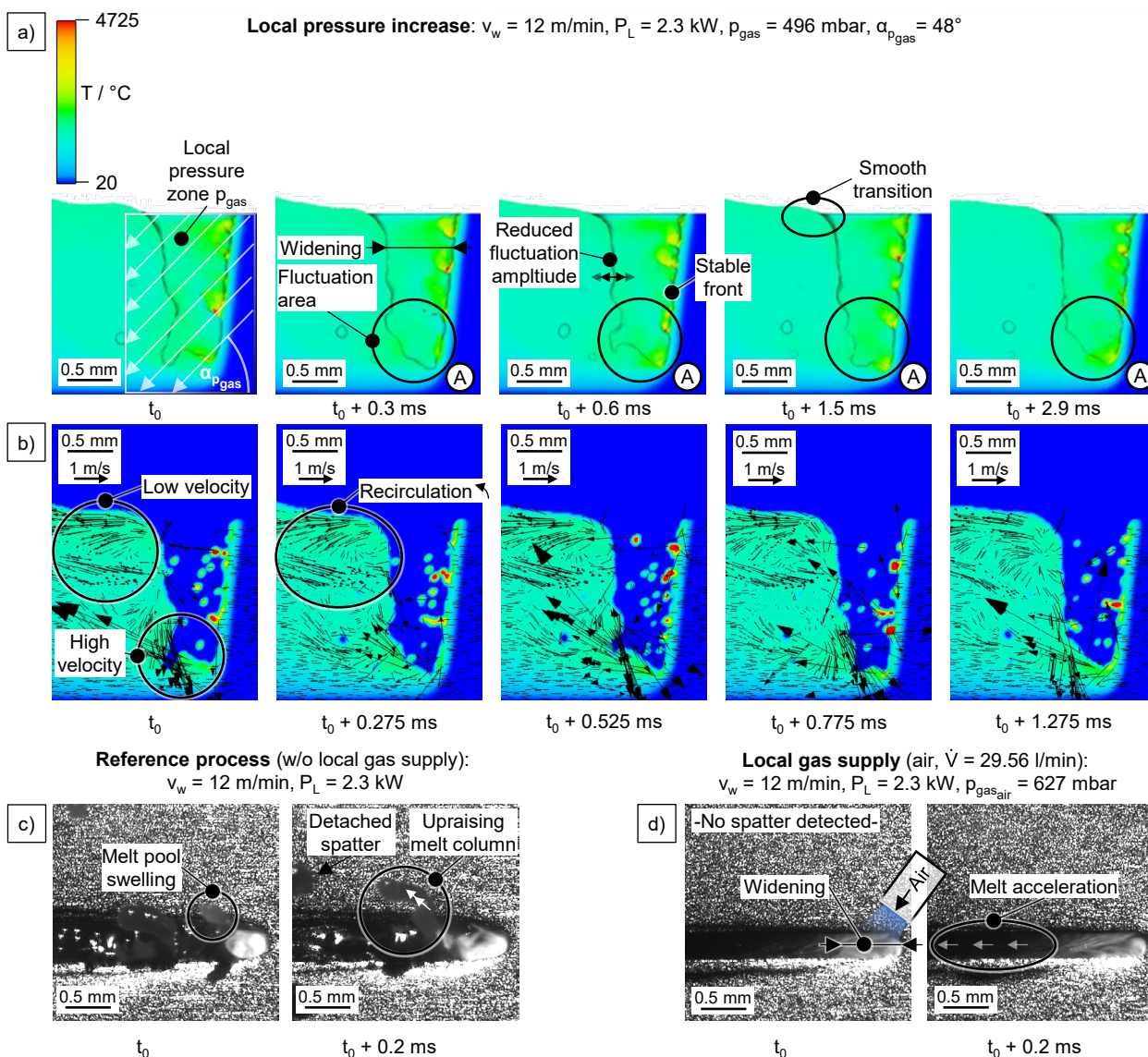


Fig. 5. Keyhole and melt pool dynamics at p_{gas} : (a) temperature field; (b) overlay of temperature and X-Z flow field; (c) high-speed videography.

preventing the formation of keyhole necking and rear-sided melt pool swellings. In contrast, no effect on the formation of the keyhole front and the lower fluctuation area of the keyhole (Fig. 5a, detail A) was observed. Pores continued to form at the keyhole bottom as a result. The described process behavior correlates with the simulated flow field (Fig. 5b). The reduced fluctuation amplitude of the keyhole rear wall resulted in a decrease of the rear-sided flow velocities within the recirculation region. In contrast, the lower part of the melt pool showed the same high flow velocities as described for the reference process. Overall, the local pressure increase resulted in a decrease in melt pool dynamics and associated spatter formation. This is confirmed by experimental investigations (Fig. 5c, d). In contrast to the significant spatter formation of the reference process (Fig. 5c), the gas-assisted process showed a significant widening of the keyhole aperture and a massively reduced spatter formation by applying an almost similar local gas flow-induced pressure of $p_{gas} = 627$ mbar (Fig. 5d). Since the numerical simulation is intended to characterize the effect of the gas flow-induced pressure increase separately, the experimental results are further affected by a gas flow-induced

momentum, which is transferred to the near-surface melt pool, resulting in an acceleration of the melt against welding direction. As a result, humps were formed at the upper surface in the experimental investigations. Since the origin of these humps is beyond the scope of this study, further information on gas flow-induced hump formation is given in [3]. Overall, the experimental results show a high level of agreement with the numerical simulation in terms of the change in keyhole dynamics and spatter formation.

4. Conclusion and outlook

This paper investigated the mechanical effect of a gas-induced pressure increase by local gas supply. While the reference process without gas supply was characterized by strong fluctuations of the keyhole rear wall (Fig. 6a, A) and a pronounced melt pool swelling at the keyhole rear wall (Fig. 6a, B), a significant reduction in fluctuation amplitude of the keyhole rear wall (Fig. 6b, A) was observed due to the local gas supply of bottled air. Further, the formation of a melt pool swelling was preserved (Fig. 6b, B), reducing the transferred momentum from the escaping metal vapor to the rear-sided

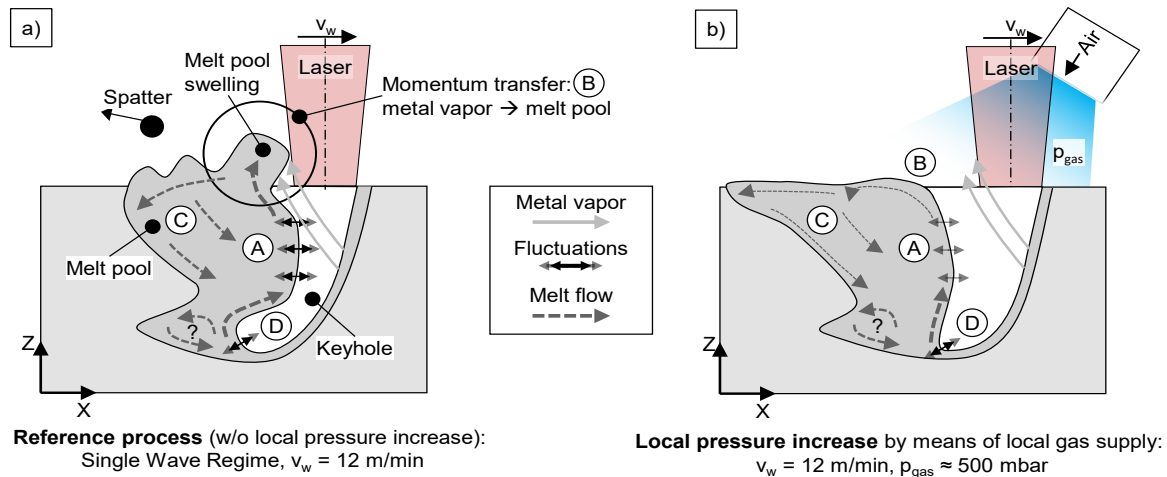


Fig. 6. Schematic model representation: (a) reference process; (b) mechanical effect of local gas supply.

melt. In addition, a reduction in flow velocities of the rear-sided melt pool recirculation was observed (Fig. 6b, C). Besides these effects, there was no effect of the gas flow-induced pressure on the fluctuation of the keyhole bottom. As a result, pores continued to form occasionally due to a keyhole collapse (not depicted in Fig. 6). However, due to some model simplifications, the CFD simulation could not represent a bulging of the keyhole bottom as observed in the high-speed synchrotron X-ray recordings and the bottom-sided recirculation of melt. Overall, the results of the numerical simulation show a high level of agreement with the results of the experimental investigation. Further investigations will focus on characterizing the dynamic keyhole behavior and determining the penetration depth of the gas.

Acknowledgements

TU Ilmenau thank ESRF – The European Synchrotron for approving the proposal (ME-1580) and the staff of beamline ID19 for their substantial support. The authors thank the Free State of Thuringia for funding the project “Leistungszentrum InSignA” (2021 FGI 0010) that allowed carrying out the experiments at ESRF.

References

- [1] Fabbro R. Melt pool and keyhole behaviour analysis for deep penetration laser welding. *Journal of Physics D: Applied Physics*. 2010;43(44):445501.
- [2] Fabbro R. Dynamic Approach Of The Keyhole And Melt Pool Behavior For Deep Penetration Nd - Yag Laser Welding. *AIP Conference Proceedings*. 2008;1047(1):18-24.
- [3] Schmidt L, Hickethier S, Schricker K, Bergmann JP. Low-spatter high speed welding by use of local shielding gas flows. *Proceedings of SPIE LASE Conference*. 2019;10911.
- [4] Schmidt L, Schricker K, Bergmann JP, Hickethier S. Effect of gas flow on spatter formation in deep penetration welding at high welding speeds. *Proceedings of Lasers in Manufacturing Conference; Munich2019*. p. 1-7.
- [5] Schmidt L, Schricker K, Bergmann JP, Junger C. Effect of Local Gas Flow in Full Penetration Laser Beam Welding with High Welding Speeds. *Applied Sciences*. 2020;10(5):1867.
- [6] Schmidt L, Schricker K, Diegel C, Sachs F, Bergmann JP, Knauer A, et al. Effect of partial and global shielding on surface-driven phenomena in keyhole mode laser beam welding. *Welding in the World*. 2023.
- [7] Kaplan AFH, Powell J. Spatter in laser welding. *Journal of Laser Applications*. 2011;23(3):032005.
- [8] Diegel C, Mattulat T, Schricker K, Schmidt L, Seefeld T, Bergmann JP, et al. Interaction between Local Shielding Gas Supply and Laser Spot Size on Spatter Formation in Laser Beam Welding of AISI 304. *Applied Sciences [Internet]*. 2023; 13(18).
- [9] Jovic G, Bormann A, Pröll J, Böhm S. Laser welding with side-gas application and its impact on spatter formation and weld seam shape. *Procedia CIRP*. 2020;94:649-54.
- [10] Schmidt L, Schricker K, Diegel C, Bergmann JP. Effect of local pressure distribution on spatter formation for welding high alloy steel at high welding speeds. *Procedia CIRP*. 2022;111:391-6.
- [11] Beck M. *Modellierung des Lasertiefschweißens*: Teubner; 1996.
- [12] Katayama S, Tsukamoto S, Fabbro R. *Handbook of laser welding technologies*: Woodhead Publishing; 2013.
- [13] Chianese G, Hayat Q, Jabar S, Franciosa P, Ceglarek D, Patalano S. A multi-physics CFD study to investigate the impact of laser beam shaping on metal mixing and molten pool dynamics during laser welding of copper to steel for battery terminal-to-casing connections. *Journal of Materials Processing Technology*. 2023;322:118202.
- [14] Mills KC. *Recommended values of thermophysical properties for selected commercial alloys*: Woodhead Publishing; 2002.
- [15] Wilthan B, Reschab H, Tanzer R, Schützenhöfer W, Pottlacher G. Thermophysical properties of a chromium–nickel–molybdenum steel in the solid and liquid phases. *International Journal of Thermophysics*. 2008;29(1):434-44.
- [16] Bogaard RH. *Thermal Conductivity of Selected Stainless Steels*. In: Ashworth T, Smith DR, editors. *Thermal Conductivity 18*. Boston, MA: Springer US; 1985. p. 175-85.
- [17] Chu TK, Ho CY. *Thermal Conductivity and Electrical Resistivity of Eight Selected AISI Stainless Steels*. In: Mirkovich VV, editor. *Thermal Conductivity 15*. Boston, MA: Springer US; 1978. p. 79-104.
- [18] Bachmann M. *Numerische Modellierung einer elektromagnetischen Schmelzbadkontrolle beim Laserstrahlschweißen von nicht-ferromagnetischen Werkstoffen [PhD Thesis]*: Technische Universität Berlin; 2014.
- [19] AISI Type 304 Stainless Steel - Physical properties [Database]. ASM Aerospace Specification Metals Inc.; 2024 [Available from: <https://asm.matweb.com/search/SpecificMaterial.asp?bassnum=MQ304A>].
- [20] Balasubramanian K, Shanmugam NS, Buvanashakaran G, Sankaranarayanan K. Numerical and experimental investigation of laser beam welding of AISI 304 stainless steel sheet. *Advances in Production Engineering & Management*. 2008;3(2):93-105.
- [21] Rader DJ, Castaneda JN, Torczynski JR, Grasser TW, Trott WM. *Measurements of thermal accommodation coefficients*. United States; 2005 2005-10-01.
- [22] Berger P, Schuster R, Hügel H, Graf T. Moving humps at the capillary front in laser welding. *International Congress on Applications of Lasers & Electro-Optics*. 2010;2010(1):39-43.